

A network based approach for unbalanced optimal transport on surfaces

Jiangong Pan^a, Wei Wan^b, Yuejin Zhang^a, Chenlong Bao^c, Zuoqiang Shi^{c,*}

^a*Yau Mathematical Sciences Center, Tsinghua University, Beijing 100084, PR China*

^b*School of Mathematics and Physics, North China Electric Power University, Beijing, China*

^c*Yau Mathematical Sciences Center, Tsinghua University, Beijing 100084, China, and YanqiLake Beijing Institute of Mathematical Sciences and Applications, Beijing 101408, China*

Abstract

In this paper, we present a neural network approach to address the dynamic unbalanced optimal transport problem on surfaces with point cloud representation. For surfaces with point cloud representation, traditional method is difficult to apply due to the difficulty of mesh generating. Neural network is easy to implement even for complicate geometry. Moreover, instead of solving the original dynamic formulation, we consider the Hamiltonian flow approach, i.e. Karush-Kuhn-Tucker system. Based on this approach, we can exploit mathematical structure of the optimal transport to construct the neural network and the loss function can be simplified. Extensive numerical experiments are conducted for surfaces with different geometry. We also test the method for point cloud with noise, which shows stability of this method. This method is also easy to generalize to diverse range of problems.

Keywords: unbalanced optimal transport, Hamiltonian flow, point cloud, neural network.

AMS subject classifications. 65K10, 68T05, 68T07

1. Introduction.

The concept of optimal transport (OT) stands as a foundational cornerstone, offering profound insights across numerous domains, including economics, physics, image processing, and machine learning [1]. At its essence, OT is concerned with devising the most efficient means of reallocating resources from source to target allocation points while minimizing associated costs. While the conventional perspective on the OT problem revolves around achieving equilibrium, wherein the total mass of the source distribution aligns precisely with the target distribution, real-world scenarios often disrupt this equilibrium, resulting in resource distributions that introduce disparities in mass. These real-world scenarios have given rise to the development of the unbalanced optimal transport (UOT) problem, an extension designed to address situations characterized by unequal source and target distribution masses [2].

In the unbalanced rendition of the OT problem, the central objective of improving efficiency and minimizing transportation costs remains unwavering. However, the introduction of varying masses introduces an additional layer of complexity, presenting both challenges and avenues for

*Corresponding author.

Email addresses: mathpjg@sina.com (Jiangong Pan), weiw@ncepu.edu.cn (Wei Wan), zhangyj19@mails.tsinghua.edu.cn (Yuejin Zhang), clbao@tsinghua.edu.cn (Chenlong Bao), zqshi@tsinghua.edu.cn (Zuoqiang Shi)

exploration. This multifaceted issue finds applications across a spectrum of fields, including image registration [3, 4, 5], transformation and generation [6, 7, 8], as well as climate modeling [9, 10, 11], style transfer [7, 12, 13], and medical imaging [14, 15, 16]. Despite achieving notable numerical successes, the UOT problem grapples with computational constraints, as diverse conditions often pose formidable challenges for conventional methods, which severely limits the applicability of UOT in different scenarios.

The origins of the OT problem can be traced back to the work of Monge in 1781 [17], where he focused on determining the minimum cost required for efficient transportation. However, solving the Monge problem directly has proven to be a formidable task, primarily due to its intricate non-convex nature and the absence of clear minimal solutions. To address this challenge, the Kantorovich problem, introduced by Kantorovich in 1942 [18], emerged as a solution by introducing a novel approach. This approach involves incorporating a joint distribution function, effectively replacing the need to solve the intricate transport map. In cases where both the source and destination of transportation are discrete, the Kantorovich problem simplifies into a conventional linear programming problem. Consequently, the simplex method [19] can be employed to tackle this problem. Nevertheless, it's important to note that the computational cost associated with these approaches can often be quite substantial.

Benamou and Brenier [20] made a groundbreaking contribution by introducing the temporal dimension into the Kantorovich problem. This innovative addition led to a transformation, turning it into a problem involving a partial differential equation (PDE) constrained optimal control. This transformation gave rise to the intriguing concept of a dynamic OT problem. Consider the model over a time interval T and a spatial region Ω . Here, ρ represents the density, and \mathbf{v} denotes the velocity of the density. In the dynamic OT problem, we are concerned with ρ , subject to given initial and terminal densities ρ_0 and ρ_1 , and (ρ, \mathbf{v}) must satisfy the mass conservation law. The primary objective of OT is to minimize the total cost across all feasible pairs of $(\rho, \mathbf{v}) \in \mathcal{C}(\rho_0, \rho_1)$. The problem can be formally stated as follows:

$$\mathcal{W}_2(\rho_0, \rho_1) = \min_{(\rho, \mathbf{v}) \in \mathcal{C}(\rho_0, \rho_1)} \int_T \int_{\Omega} \frac{1}{2} \rho(t, \mathbf{x}) \|\mathbf{v}(t, \mathbf{x})\|^2 d\mathbf{x} dt, \quad (1)$$

where

$$\mathcal{C}(\rho_0, \rho_1) := \{(\rho, \mathbf{v}) : \partial_t \rho + \operatorname{div}(\rho \mathbf{v}) = 0, \rho(0, \mathbf{x}) = \rho_0(\mathbf{x}), \rho(1, \mathbf{x}) = \rho_1(\mathbf{x})\}. \quad (2)$$

It is noteworthy that the resulting PDE predominantly consists of continuity equations, establishing an inherent connection with fluid mechanics. This intrinsic link with fluid mechanics broadens the range of potential applications, expanding the scope of the problem to encompass areas such as unnormalized OT [21, 22, 23] and mean field games [24, 25, 26].

Introducing the source term into the continuity equation and modifying the optimization objective to the Wasserstein-Fisher-Rao (WFR) metric eliminates the constraint of mass conservation, thereby leading us to the dynamic UOT problem. In recent years, significant progress has been made in the field of OT and its related areas. Gerber et al. [27] applied optimal transport to the analysis of brain pathologies, considering changes in shape and alterations in brain matter. Subsequently, Gallouët et al. [28] explored alternating minimizing movements for the Wasserstein distance and Fisher-Rao distance, particularly in the context of systems involving multiple interacting species. Kondratyev et al. [29] investigated gradient flow over the space of Radon measurements using the Hellinger-Kantorovich distance, revealing new isoperimetric-type functional inequalities

that govern relative entropies. Sato et al. [30] delved into the computational complexity of the Kantorovich-Rubinstein distance and optimal partial transport, proposing an algorithm for the UOT problem. Another significant development was the introduction of the Sinkhorn algorithm by Pham’s team [31], which addressed the entropic regularized UOT problem. The algorithm’s complexity was established to be of order $O(n^2/\epsilon)$ for an ϵ -approximate solution. Chapel et al. [32] brought novel insights, leveraging inverse problems and nonnegative matrix factorization for solving the non-negative penalized linear regression problem, which aligns with the concepts of OT. Li and his team [33] harnessed UOT with Kullback-Leibler divergence to counter the cycle-skipping artifact in full waveform inversion. Bauer et al. [34], also this year, unveiled the relationship between the square root normal field shape distance and the WFR UOT distance. Further advancements were witnessed as Séjourné et al. [35] introduced a provably accelerated Sinkhorn algorithm and proposed a Frank-Wolfe solver for the translation invariant formulation of UOT. Looking to the most recent developments, Beier and his team [36] tackled the unbalanced multi-marginal OT problem, establishing the existence of a unique OT plan and extending the Sinkhorn algorithm to the multi-marginal setting while proving its convergence. These collective efforts demonstrate the increasing importance of UOT in various scientific fields. But none of them can be effectively extended to the point cloud problem, which will be the core of the main research in this paper.

In this paper, we introduce an innovative neural network approach based on the Hamiltonian flow formulation. Comparing with the dynamic formulation, Hamiltonian flow reveals intrinsic connection between the velocity field and the potential function, which reduce the complexity of the neural networks. And the loss function can be simplified also.

The rest of our paper is organized as follows. In section 2, we give some relevant work on solving UOT problems in recent years. We generalize the UOT problem to obtain the dynamic manifolds UOT problem, and obtain its equivalent form using KKT conditions in Section 3. Next, we discretize the problem and establish the corresponding loss function. Experimental results and implementation details are given in Section 5. Finally, the conclusion of this paper is placed by us in Section 6.

2. Related work.

In recent years, the field of deep learning has showcased extraordinary achievements across a diverse spectrum of computational challenges. These achievements span from tasks like image classification [37, 38, 39], speech recognition [40, 41, 42], natural language processing [43, 44, 45], numerical approximations of PDE [46, 47, 48] and the generation of images [49, 50, 51]. The success of these applications suggests that we can also use deep learning to solve UOT problems. In 2018, Yang et al. [52] proposed a scalable UOT method, combining it with neural generative models, specifically Generative Adversarial Networks. Moving forward, in 2020, Lee et al. [53] introduced a novel UOT regularizer formulation with linear optimization-variable complexity, effectively addressing challenges in the inverse imaging problem. Building upon these innovations, in 2021, Ma et al. [54] harnessed UOT distance to quantify discrepancies between predicted density maps and point annotations, highlighting its robustness against spatial perturbations. In the same year, Le et al. [55] employed UOT as a solution to the unbalanced assignment problem in multi-camera tracking, showcasing its versatility. Additionally, Fatras et al. [56] enhanced robustness through a mini-batch strategy and UOT on large-scale datasets, advancing its practicality in 2021. Progressing to 2022, Cao et al. [57] proposed uniPort, a unified single-cell data integration framework, which effectively manages data heterogeneity across datasets using a coupled variational autoencoder and

minibatch unbalanced optimal transport. This scalability extends to large-scale datasets, further enhancing its utility. In the same year, Lübeck et al. [8] developed NUBOT, a semi-coupling based formalism addressing mass creation and destruction, along with an algorithmic scheme derived through a cycle-consistent training procedure. Venturing into 2023, Shen and his team [58] introduced UOTSumm, a pioneering framework for long document summarization. Unlike conventional approaches reliant on biased tools like Rouge, UOTSumm adopts UOT principles to directly learn text alignment from summarization data, rendering it adaptable to existing neural abstractive text summarization models. Similarly, De et al. [59] demonstrated the applicability of UOT in object detection in the same year, achieving state-of-the-art results in both average precision and average recall metrics, while also accelerating initial convergence. Furthermore, in 2023, Dan and colleagues [60] presented Uncertainty-Guided Joint UOT, a comprehensive framework addressing feature distribution alignment and uncertainty posed by noisy training samples through a feature uncertainty estimation mechanism and UOT strategy.

3. Dynamic formulation of UOT

First, we briefly review the dynamic formulation of UOT in Euclidean space. Considering a modeling framework that operates over the time interval $[0, 1]$ and a spatial domain denoted as $\Omega \in \mathbb{R}^d$. Here, $\rho : [0, 1] \times \Omega \rightarrow \mathbb{R}^+$ defines the density distribution of agent across time $t \in [0, 1]$ and space. The velocity field $\mathbf{v} = (v_1, \dots, v_d) : [0, 1] \times \Omega \rightarrow \mathbb{R}^d$ characterizes the agent’s strategy (or control) to affect the evolution of this density. Introducing $g : [0, 1] \times \Omega \rightarrow \mathbb{R}$, a scalar field, which captures the mass growth and depletion. The primary goal of the UOT problem is to effectively reduce the combined costs linked to all permissible pairs of (ρ, \mathbf{v}, g) that adhere to the limitations stipulated by $\mathcal{C}(\rho_0, \rho_1)$. This complex undertaking is conceptualized through the WFR metric:

$$\mathcal{W}_{WFR}(\rho_0, \rho_1) = \min_{(\rho, \mathbf{v}, g) \in \mathcal{C}(\rho_0, \rho_1)} \int_0^1 \int_{\Omega} \frac{1}{2} \rho(t, \mathbf{x}) \|\mathbf{v}(t, \mathbf{x})\|^2 + \frac{1}{\eta} \rho(t, \mathbf{x}) g(t, \mathbf{x})^2 d\mathbf{x} dt, \quad (3)$$

where

$$\mathcal{C}(\rho_0, \rho_1) := \{(\rho, \mathbf{v}, g) : \partial_t \rho + \text{div}(\rho \mathbf{v}) = \rho g, \rho(0, \mathbf{x}) = \rho_0(\mathbf{x}), \rho(1, \mathbf{x}) = \rho_1(\mathbf{x})\}, \quad (4)$$

and η is a source coefficient which can balance transport and creation/destruction of mass. It is not difficult to find that when $g(t, \mathbf{x}) = 0$, problem (3) and (4) will degenerate into (1) and (2) respectively.

In this article, we focus on solving dynamic UOT problems on manifolds. Naturally, we need to extend the dynamic UOT to manifolds and call it the dynamic manifolds UOT (MUOT). In recent years, some researchers have also paid attention to this aspect. Lavenant et al. [61] introduced a groundbreaking methodology that involves interpolating between probability distributions on discrete surfaces, leveraging the principles of optimal transport theory. This innovative technique not only maintains the structural integrity of the data but also engenders the development of a Riemannian metric within the domain of probability distributions pertaining to discrete surfaces. Yu et al. [62] have elegantly demonstrated the profound connection between systems of partial differential equations and optimal conditions for correlated variational forms on intricate manifolds. Moreover, they have ingeniously crafted a proximal gradient method tailored for addressing variational mean-field games.

We consider a mathematical model defined over the time interval $[0, 1]$, operating within a compact surface $\Gamma \subset \mathbb{R}^3$. In this paper, we focus on closed surfaces, i.e., $\partial\Gamma = \emptyset$. Let $\rho : [0, 1] \times \Gamma \rightarrow \mathbb{R}^+$ denote the density of agents as a function of time $t \in [0, 1]$. The density values are constrained to the positive real numbers. Additionally, let $\mathbf{v} = (v_1, \dots, v_d) \in T(\Gamma) : [0, 1] \times \Gamma \rightarrow \mathbb{R}^d$ represent the velocity field associated with the density. The velocity field represents the movement of the mass. Here, $g : [0, 1] \times \Gamma \rightarrow \mathbb{R}$ represents a scalar field that characterizes the local growth and depletion of mass within the system. Our main focus is on understanding the behavior of (ρ, \mathbf{v}, g) given ρ_0 and ρ_1 densities. Then, the dynamic MUOT can be expressed as

$$\mathcal{W}_M(\rho_0, \rho_1) = \min_{(\rho, \mathbf{v}, g) \in \mathcal{C}(\rho_0, \rho_1)} \int_0^1 \int_{\Gamma} \frac{1}{2} \rho(t, \mathbf{x}) \|\mathbf{v}(t, \mathbf{x})\|^2 + \frac{1}{\eta} \rho(t, \mathbf{x}) g(t, \mathbf{x})^2 d\sigma dt, \quad (5)$$

where

$$\mathcal{C}(\rho_0, \rho_1) := \{(\rho, \mathbf{v}, g) : \partial_t \rho + \operatorname{div}_{\Gamma}(\rho \mathbf{v}) = \rho g, \rho(0, \mathbf{x}) = \rho_0(\mathbf{x}), \rho(1, \mathbf{x}) = \rho_1(\mathbf{x})\}, \quad (6)$$

and η is a source coefficient which can balance transport and creation/destruction of mass. Let \mathbf{n} denote the outward normal vector of the surface Γ , and \mathcal{I} be the identity operator,

$$P(\mathbf{x}) = \mathcal{I} - \mathbf{n}(\mathbf{x})\mathbf{n}(\mathbf{x})^T$$

represents the projection operator of the three-dimensional vector at node \mathbf{x} of the manifolds to its tangent component, and the tangential gradient operator, tangential divergence operator at node \mathbf{x} are respectively defined

$$\nabla_{\Gamma} = P(\mathbf{x})\nabla, \quad \operatorname{div}_{\Gamma} = \operatorname{trace}(\nabla_{\Gamma}).$$

For dynamic optimal transport on \mathbb{R}^d , it is well known that it can be solved by Hamiltonian flow which is actually Karush-Kuhn-Tucker (KKT) conditions of the dynamic optimal transport.

For unbalanced optimal transport on manifold, we can also get corresponding Hamiltonian flow based on KKT condition.

Theorem 1. *Suppose $(\hat{\rho}, \hat{\mathbf{v}}, \hat{g}, \hat{\phi}, \hat{\phi}_1, \hat{\phi}_2)$ is a saddle point of (7),*

$$\begin{aligned} L(\rho, \mathbf{v}, g, \phi, \phi_1, \phi_2) &= \int_0^1 \int_{\Gamma} \frac{1}{2} \rho(t, \mathbf{x}) \|\mathbf{v}(t, \mathbf{x})\|^2 + \frac{1}{\eta} \rho(t, \mathbf{x}) g(t, \mathbf{x})^2 d\sigma dt \\ &+ \int_0^1 \int_{\Gamma} \phi(t, \mathbf{x}) [\partial_t \rho(t, \mathbf{x}) + \operatorname{div}_{\Gamma}(\rho(t, \mathbf{x}) \mathbf{v}(t, \mathbf{x})) - \rho(t, \mathbf{x}) g(t, \mathbf{x})] d\sigma dt \\ &+ \int_{\Gamma} \phi_1(\mathbf{x}) (\rho(0, \mathbf{x}) - \rho_0(\mathbf{x})) d\sigma + \int_{\Gamma} \phi_2(\mathbf{x}) (\rho(1, \mathbf{x}) - \rho_1(\mathbf{x})) d\sigma. \end{aligned} \quad (7)$$

Then, solution $(\hat{\rho}, \hat{\phi})$ (where $\hat{\mathbf{v}} = \nabla_{\Gamma} \hat{\phi}$ and $\hat{g} = \frac{\eta}{2} \hat{\phi}$) of (8) is the optimal solution for (5) and (6). And we refer to (8) as dynamic KKT-MUOT:

$$\begin{aligned} \partial_t \rho + \operatorname{div}_{\Gamma}(\rho \nabla_{\Gamma} \phi) &= \frac{\eta}{2} \rho \phi, \quad (t, \mathbf{x}) \in (0, 1) \times \Gamma, \\ \partial_t \phi + \frac{1}{2} \|\nabla_{\Gamma} \phi\|^2 &= -\frac{\eta}{4} \phi^2, \quad (t, \mathbf{x}) \in [0, 1] \times \Gamma, \\ \rho(0, \mathbf{x}) &= \rho_0(\mathbf{x}), \quad \rho(1, \mathbf{x}) = \rho_1(\mathbf{x}), \quad \mathbf{x} \in \Gamma. \end{aligned} \quad (8)$$

Proof. Performing a simple partition integral over (7), we get

$$\begin{aligned}
L(\rho, \mathbf{v}, g, \phi, \phi_1, \phi_2) &= \int_0^1 \int_{\Gamma} \frac{1}{2} \rho(t, \mathbf{x}) \|\mathbf{v}(t, \mathbf{x})\|^2 + \frac{1}{\eta} \rho(t, \mathbf{x}) g(t, \mathbf{x})^2 d\sigma dt \\
&+ \int_{\Gamma} (\phi(1, \mathbf{x}) \rho(1, \mathbf{x}) - \phi(0, \mathbf{x}) \rho(0, \mathbf{x})) d\sigma - \int_0^1 \int_{\Gamma} \partial_t \phi(t, \mathbf{x}) \rho(t, \mathbf{x}) d\sigma dt \\
&- \int_0^1 \int_{\Gamma} \nabla_{\Gamma} \phi(t, \mathbf{x}) \cdot (\rho(t, \mathbf{x}) \mathbf{v}(t, \mathbf{x})) + \phi(t, \mathbf{x}) \rho(t, \mathbf{x}) g(t, \mathbf{x}) d\sigma dt \\
&+ \int_{\Gamma} \phi_1(\mathbf{x}) (\rho(0, \mathbf{x}) - \rho_0(\mathbf{x})) d\sigma + \int_{\Gamma} \phi_2(\mathbf{x}) (\rho(1, \mathbf{x}) - \rho_1(\mathbf{x})) d\sigma.
\end{aligned} \tag{9}$$

Then computing the saddle point of the above equation, we have

$$\begin{aligned}
L_{\rho} = 0 &\Rightarrow \partial_t \phi(t, \mathbf{x}) + \nabla_{\Gamma} \phi(t, \mathbf{x}) \cdot \mathbf{v}(t, \mathbf{x}) + \phi(t, \mathbf{x}) g(t, \mathbf{x}) - \frac{1}{2} \|\mathbf{v}(t, \mathbf{x})\|^2 - \frac{1}{\eta} g(t, \mathbf{x})^2 = 0, \\
L_{\mathbf{v}} = 0 &\Rightarrow \mathbf{v}(t, \mathbf{x}) - \nabla_{\Gamma} \phi(t, \mathbf{x}) = 0, \\
L_g = 0 &\Rightarrow \frac{2}{\eta} g(t, \mathbf{x}) - \phi(t, \mathbf{x}) = 0.
\end{aligned} \tag{10}$$

Next, we obtain

$$\partial_t \phi + \frac{1}{2} \|\nabla_{\Gamma} \phi\|^2 + \frac{\eta}{4} \phi^2 = 0, \tag{11}$$

with $\mathbf{v} = \nabla_{\Gamma} \phi$ and $g = \frac{\eta}{2} \phi$. □

In the subsequent section, we will introduce the neural network approach to solve (8).

4. Neural Network approach

In this paper, we use a fully connected deep neural network (FCDNN) as an approximation function. FCDNN is a type of network in which two adjacent layers of neurons in a network are connected to each other. Like common neural networks, it includes neurons, weights, biases, and activation functions. Through the use of known data, the weights and biases are constantly trained to obtain the optimal approximation function. Now let's use FCDNN to approximate ρ, ϕ :

$$\begin{aligned}
\rho(t, \mathbf{x}) &= \rho_{NN}(t, \mathbf{x}; \theta) = \mathcal{N}_M \mathcal{N}_{M-1} \mathcal{N}_{M-2} \cdots \mathcal{N}_1 \mathcal{N}_0(\mathbf{x}), \\
\phi(t, \mathbf{x}) &= \phi_{NN}(t, \mathbf{x}; \zeta) = \mathcal{N}_M \mathcal{N}_{M-1} \mathcal{N}_{M-2} \cdots \mathcal{N}_1 \mathcal{N}_0(\mathbf{x}),
\end{aligned} \tag{12}$$

where \mathbf{x} is the Cartesian coordinate, M is the number of layers of the neural network and $M > 0$ and

$$\begin{cases} \mathcal{N}_0(\mathbf{x}) = \mathbf{x}, \\ \mathcal{N}_m(\mathbf{x}) = \sigma(W_m \mathcal{N}_{m-1}(\mathbf{x}) + b_m), \quad \text{for } 1 \leq m \leq M-1, \\ \mathcal{N}_M(\mathbf{x}) = W_M \mathcal{N}_{M-1}(\mathbf{x}) + b_M. \end{cases} \tag{13}$$

$W_m, b_m (1 \leq m \leq M)$ are parameters to be trained. And σ is given activation function. In the subsequent numerical experiments, we use

$$\sigma(\mathbf{x}) = \tanh(\mathbf{x})$$

for ϕ_{NN} . To ensure that the ρ is non-negative, we use the Softplus function

$$\sigma(\mathbf{x}) = \log(1 + e^{\mathbf{x}})$$

in the output layer of $\rho_{NN}(t, \mathbf{x}; \theta)$.

The surface is given by point cloud $\{\mathbf{x}_j\}_{j=1}^N$. Moreover, we assume the associate out normal $\{\mathbf{n}_j\}_{j=1}^N$ is also given. In addition, we need to discretize time by $0 = t^0 < t^1 < \dots < t^{n-1} < t^n < \dots < t_t^N = T$.

With the approximation of FCDNN to ρ and ϕ , then we need to consider how to update the parameter. Before using the optimization algorithm, we need to establish the corresponding optimization objective, that is, the loss function (also known as the objective function). For KKT-MUOT problem (8), the following loss function is established:

$$\mathcal{L}_{MUOT}(\theta, \zeta) = \lambda_c \mathcal{L}_c(\theta, \zeta) + \lambda_{hj} \mathcal{L}_{hj}(\zeta) + \lambda_{ic} \mathcal{L}_{ic}(\theta), \quad (14)$$

where

$$\begin{aligned} \mathcal{L}_c(\theta, \zeta) &= \frac{1}{N_c} \sum_{i=1}^{N_c} \|\partial_t \rho(t_i, \mathbf{x}_i; \theta) + \text{div}_\Gamma(\rho(t_i, \mathbf{x}_i; \theta) \nabla_\Gamma \phi(t_i, \mathbf{x}_i; \zeta)) - \frac{\eta}{2} \rho(t_i, \mathbf{x}_i; \theta) \phi(t_i, \mathbf{x}_i; \zeta)\|^2, \\ \mathcal{L}_{hj}(\zeta) &= \frac{1}{N_{hj}} \sum_{i=1}^{N_{hj}} \|\partial_t \phi(t_i, \mathbf{x}_i; \zeta) + \|\nabla_\Gamma \phi(t_i, \mathbf{x}_i; \zeta)\|^2 + \frac{\eta}{4} \phi(t_i, \mathbf{x}_i; \zeta)^2\|^2, \\ \mathcal{L}_{ic}(\theta) &= \frac{1}{N_{ic}} \sum_{i=1}^{N_{ic}} (\|\rho(0, \mathbf{x}_i; \theta) - \rho_0(\mathbf{x}_i)\|^2 + \|(\rho(1, \mathbf{x}_i; \theta) - \rho_1(\mathbf{x}_i))\|^2), \end{aligned} \quad (15)$$

where λ_c , λ_{hj} and λ_{ic} are the weighting coefficients for different loss terms; N_c , N_{hj} and N_{ic} are the numbers of data points for different terms. Various differential operators in the loss function can be computationally obtained by automatic differentiation techniques [63]. In this paper, we use the Adam optimizer [64], an adaptive algorithm for gradient-based first-order optimization, to optimize the model parameters.

5. Numerical Experiments.

In this section, we perform a total of five arithmetic cases to verify the effectiveness of the proposed algorithm. The calculations are first performed in the most classical Gaussian example in two dimension. Then the source term coefficients in the UOT problem are explored in the case of the UOT problem, considering different degrees of source terms, and their impact on the transport scheme. Next, we consider the UOT problem on manifolds. And we studied the MOT and MUOT problems on various stream forms with different topology. Further, we consider adding different degrees of Gaussian noise to the point cloud to verify the robustness of our algorithm. Finally, three different shape transport experiments were carried out, by calculating between different patterns, in order to obtain the whole transport scheme. In experiment, if Euclidean space is considered, we need the space boundary condition

$$\rho v \cdot \mathbf{n} = 0.$$

5.1. Gaussian Examples

In this section, we perform numerical experiments on classical Gaussian examples and mixed Gaussian examples on two dimension (2D) spaces using the proposed algorithm to verify the effectiveness.

Two classical examples and the corresponding configurations are given in Table 5.1.1, where Gaussian density function is

$$\rho_G(\mathbf{x}, \mu, \Sigma) = \frac{1}{(2\pi)^{1/2} |\Sigma|^{1/2}} e^{-\frac{1}{2}(\mathbf{x}-\mu)^T \Sigma^{-1}(\mathbf{x}-\mu)}.$$

The parameters $\lambda_c = \lambda_{hj} = \lambda_{ic} = 1000$ and $\eta = 2$ are used in this test. We use uniform grid to sample 10 points at time t and 900 points in space (coordinate (x, y)).

Table 5.1.1: Initial distribution $\rho_0(\mathbf{x})$, target distribution $\rho_1(\mathbf{x})$ for 2D KKT-UOT.

Test	$\rho_0(\mathbf{x})$	$\rho_1(\mathbf{x})$
A	$\rho_G(\mathbf{x}, [0.4, 0.4], 0.01 \cdot \mathbf{I})$	$2\rho_G(\mathbf{x}, [0.6, 0.6], 0.005 \cdot \mathbf{I})$
B	$\rho_G(\mathbf{x}, [0.5, 0.5], 0.005 \cdot \mathbf{I})$	$\rho_G(\mathbf{x}, [0.3, 0.3], 0.005 \cdot \mathbf{I}) + \rho_G(\mathbf{x}, [0.7, 0.3], 0.005 \cdot \mathbf{I})$ $+ \rho_G(\mathbf{x}, [0.7, 0.7], 0.005 \cdot \mathbf{I}) + \rho_G(\mathbf{x}, [0.3, 0.7], 0.005 \cdot \mathbf{I})$

As shown in Figures 5.1.1, our method performs well in simple Gaussian translations. In the mixed Gaussian splitting, KKT-OT can also divide as expected.

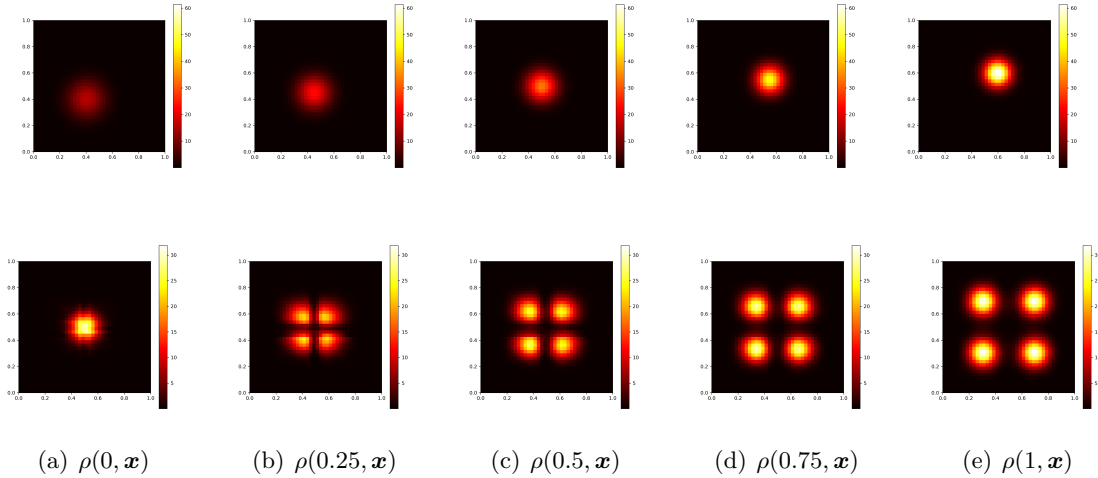


Figure 5.1.1: 2D KKT-UOT test. First row: Simple gaussian transport. Second row: Mixed gaussian split transport.

In addition, we give the values of the residuals of the equations in each loss function for Gaussian examples in Table 5.1.2. By observing the experimental results, we can know that for simple types of Gaussian shift problems, the residuals of the equations are very small, which means that our algorithm performs very well. But in test B, loss is relatively high since test B is more complicated than test A.

In UOT problem (3), there is a parameter η . This coefficient controls the creation or destruction of mass during transport. When $\eta \rightarrow 0$, the UOT solution is supposed to converge to the OT

Table 5.1.2: Loss value for Gaussian examples.

Test	KKT-OT		
	\mathcal{L}_c	\mathcal{L}_{hj}	\mathcal{L}_{ic}
A	1.50e-2	6.89e-3	5.16e-3
B	3.43e-2	5.46e-2	3.06e-2

solution. When $\eta \rightarrow \infty$, there should be no transportation at all. In next example, we will investigate effect of η .

In Test C, we set the parameters $\lambda_c = \lambda_{hj} = 100$, $\lambda_{ic} = 1000$. We select different η to test, $\eta = 10^2, 1, 10^{-6}$. The configurations of ρ_0 and ρ_1 are in Table 5.1.3. We also use uniform grid to sample 10 points at time t and 800 points in space (coordinate x).

Table 5.1.3: UOT with Variable Coefficients.

Test	$\rho_0(x)$	$\rho_1(x)$
C	$\rho_G(x, 0.7, 0.005)$	$0.3\rho_G(x, 0.7, 0.005) + 0.7\rho_G(x, 1.3, 0.005)$

The results for different η are shown in Figure 5.1.2 and the results fit the expectation very well. When η is large, the algorithm chooses generation over transport. When η is equal to 1, generation and transport are balanced at this point, matching the experimental phenomenon. When η is small, the algorithm prefers transport and almost no generation and the result almost reduce to OT. The study of different η shows that our algorithm is effective in computing UOT problems with different generation and transport requirements.

5.2. OT on point cloud

In this section, we compute the UOT problems on point cloud. We consider both OT problem $g(t, \mathbf{x}) = 0$ and the general UOT problem $g(t, \mathbf{x}) \neq 0$.

First, we consider the OT problems on simple manifolds as follows:

- *Sphere*:

$$\left(x - \frac{1}{2}\right)^2 + \left(y - \frac{1}{2}\right)^2 + \left(z - \frac{1}{2}\right)^2 = \frac{1}{4}.$$

- *Ellipsoid*:

$$\left(x - \frac{1}{2}\right)^2 + 3\left(y - \frac{1}{2}\right)^2 + 6\left(z - \frac{1}{2}\right)^2 = \frac{1}{4}.$$

- *Peanut*:

$$\left(\left(4\left(x - \frac{1}{2}\right) - 1\right)^2 + 8\left(y - \frac{1}{2}\right)^2 + 8\left(z - \frac{1}{2}\right)^2\right) \left(\left(4\left(x - \frac{1}{2}\right) + 1\right)^2 + 8\left(y - \frac{1}{2}\right)^2 + 8\left(z - \frac{1}{2}\right)^2\right) = \frac{6}{5}.$$

- *Torus*:

$$\left(0.3 - \sqrt{\left(x - \frac{1}{2}\right)^2 + \left(y - \frac{1}{2}\right)^2}\right)^2 + \left(z - \frac{1}{2}\right)^2 = \frac{1}{25}.$$

- *Opener*:

$$\left(3\left(x - \frac{1}{2}\right)^2\left(1 - 5\left(x - \frac{1}{2}\right)^2\right) - 5\left(y - \frac{1}{2}\right)^2\right)^2 + 5\left(z - \frac{1}{2}\right)^2 = \frac{1}{60}.$$

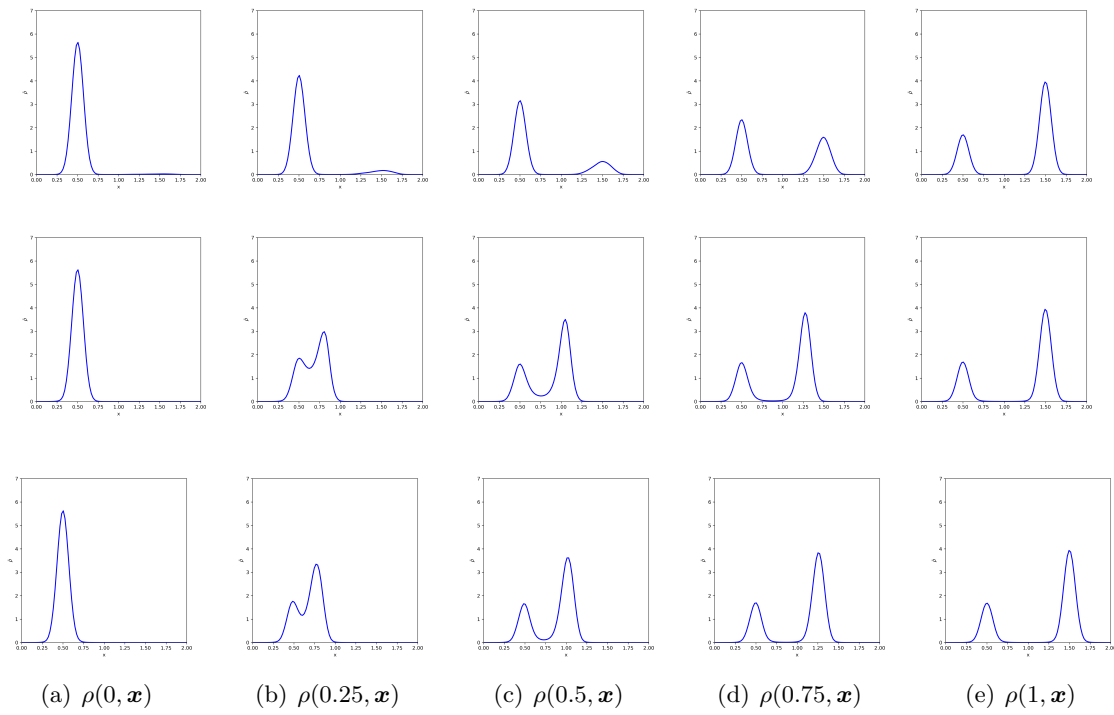


Figure 5.1.2: Variable Coefficients UOT: Numerical results for different η , from top to bottom each line $\eta = 10^2, 1, 10^{-6}$.

As can be found in Table 5.2.1, we give the settings of the initial distribution $\rho_0(\mathbf{x})$ and the terminating distribution $\rho_1(\mathbf{x})$ on different manifolds, where Gaussian density function on manifolds in [65] is defined as

$$\hat{\rho}_G(\mathbf{x}, \mu, \sigma) = ce^{-\frac{\|\mu - \mathbf{x}\|^2}{\sigma}},$$

and c is a constant. In this article, we consider $c = 100$. In addition to this, we choose $\eta = 2$ and $\lambda_c = \lambda_{hj} = 1$, $\lambda_{ic} = 1000$. And we use uniform point picking to sample 10 points at time t , isosurface method to sample 1158, 1222, 1430, 2120 and 1410 points on each surface (coordinate (x, y, z)). Isosurface method is to generate a large number of mesh nodes according to uniform sampling in three-dimensional space. Then calculate isosurface according to surface expression. And finally extract surface nodes.

Table 5.2.1: Initial distribution $\rho_0(\mathbf{x})$, target distribution $\rho_1(\mathbf{x})$ for MOT testing.

Test	$\rho_0(\mathbf{x})$	$\rho_1(\mathbf{x})$
Sphere	$\hat{\rho}_G(\mathbf{x}, [0.5, 0.5, 0], 0.01 \cdot \mathbf{I})$	$\hat{\rho}_G(\mathbf{x}, [0.5, 0.5, 1], 0.01 \cdot \mathbf{I})$
Ellipsoid	$\hat{\rho}_G(\mathbf{x}, [0.5, 0.5, \frac{6+\sqrt{6}}{12}], 0.01 \cdot \mathbf{I})$	$\hat{\rho}_G(\mathbf{x}, [0.5, 0.5, \frac{6-\sqrt{6}}{12}], 0.01 \cdot \mathbf{I})$
Peanut	$\hat{\rho}_G(\mathbf{x}, [\frac{2+\sqrt{1+\sqrt{\frac{6}{5}}}}{4}, 0.5, 0.5], 0.01 \cdot \mathbf{I})$	$\hat{\rho}_G(\mathbf{x}, [\frac{2+\sqrt{1-\sqrt{\frac{6}{5}}}}{4}, 0.5, 0.5], 0.01 \cdot \mathbf{I})$
Torus	$\hat{\rho}_G(\mathbf{x}, [\frac{5+4\sqrt{\frac{1}{2}}}{10}, \frac{5+4\sqrt{\frac{1}{2}}}{10}, 0.5], 0.01 \cdot \mathbf{I})$	$\hat{\rho}_G(\mathbf{x}, [\frac{5-4\sqrt{\frac{1}{2}}}{10}, \frac{5-4\sqrt{\frac{1}{2}}}{10}, 0.5], 0.01 \cdot \mathbf{I})$
Opener	$\hat{\rho}_G(\mathbf{x}, [\frac{1+\sqrt{\frac{1+\sqrt{1+2\sqrt{\frac{1}{15}}}}}{10}}{2}, 0.5, 0.5], 0.01 \cdot \mathbf{I})$	$\hat{\rho}_G(\mathbf{x}, [0.5, \frac{1-\sqrt{\frac{1+\sqrt{1+2\sqrt{\frac{1}{15}}}}}{10}}{2}, 0.5], 0.01 \cdot \mathbf{I})$

The results are shown in Figures 5.2.1. In these cases, the ground truth is not known, so we can not compare the numerical solutions with the exact ones. However, the neural network based method still is capable to capture the phenomena that the mass is transported along the geodesics, which suggest that our method captures the main character of the solution. The loss given in Table 5.3.2 also verifies the effectiveness of our method.

5.3. UOT on point cloud

With the success of the MOT described above, we next turn our attention to the MUOT. The mixed Gaussian UOT problem on the *sphere* is taken as our main object of study. We set the configuration of $\rho_0(\mathbf{x})$ and $\rho_1(\mathbf{x})$ in Table 5.3.1. And we use uniform point picking to sample 10 points at time t , isosurface method to sample 1158 points on Sphere (coordinate (x, y, z)). The main parameters are set by us to $\eta = 2$ and $\lambda_c = \lambda_{hj} = 1$, $\lambda_{ic} = 1000$. Also back to the mixed Gaussian function as:

$$\begin{aligned} \rho_{MG}(\mathbf{x}) = & \frac{1}{2}\hat{\rho}_G(\mathbf{x}, [0.5, 0, 0.5], 0.01 \cdot \mathbf{I}) + \frac{1}{2}\hat{\rho}_G(\mathbf{x}, [0.5, 1, 0.5], 0.01 \cdot \mathbf{I}) \\ & + \frac{1}{2}\hat{\rho}_G(\mathbf{x}, [0, 0.5, 0.5], 0.01 \cdot \mathbf{I}) + \frac{1}{2}\hat{\rho}_G(\mathbf{x}, [1, 0.5, 0.5], 0.01 \cdot \mathbf{I}). \end{aligned} \quad (16)$$

In Figure 5.3.1, we give two different examples for the merging and splitting of mixed Gaussian. The initial and terminal distribution have different mass, unbalanced optimal transport is still capable to match two distributions due to the help of the mass generation term. However, in Figure 5.3.1, merging and splitting process are not exact symmetric which means that the training of neural network may be stacked in a local minimum. Furthermore, here we are considering the

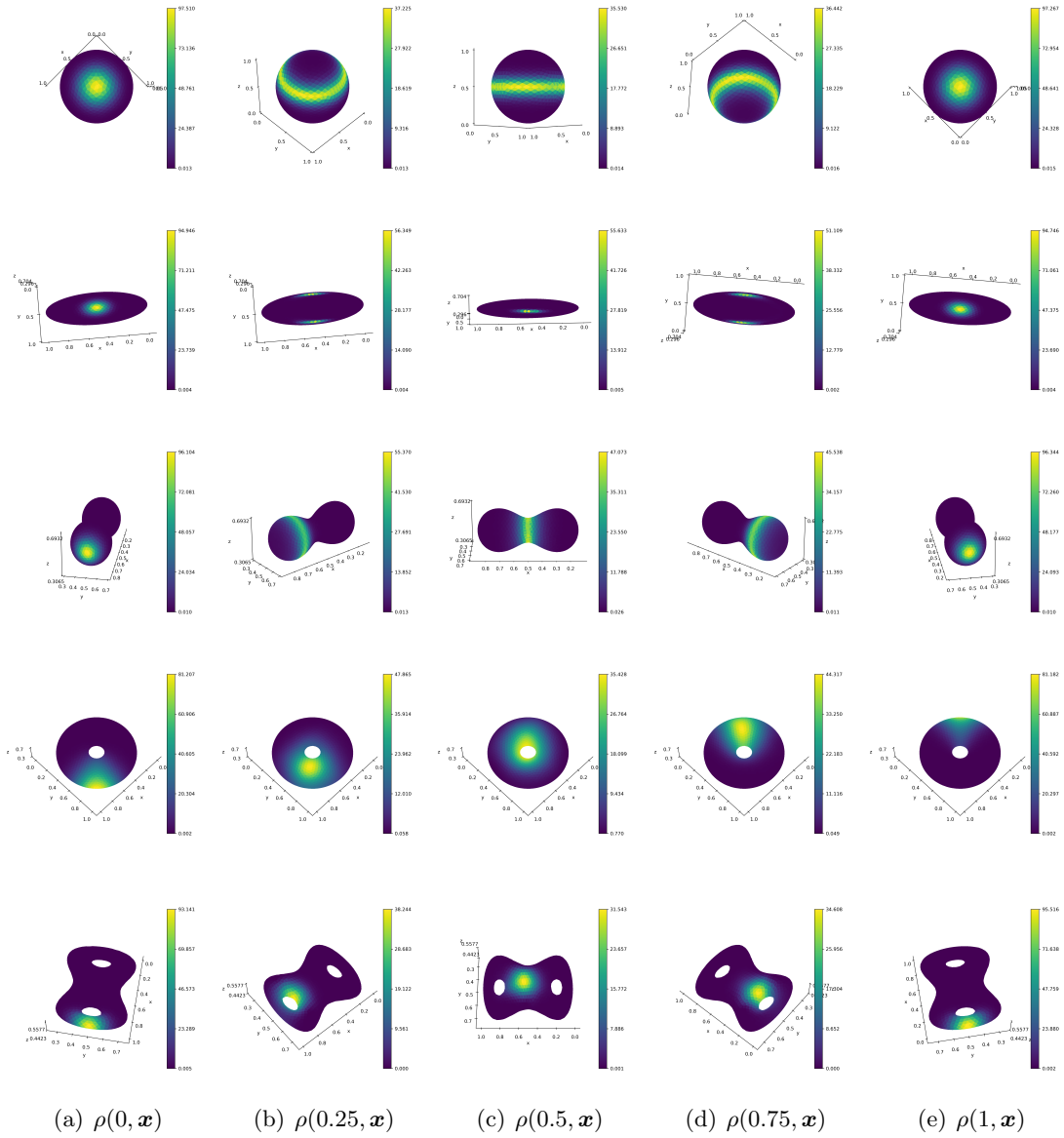


Figure 5.2.1: OT tests on point cloud.

Table 5.3.1: Initial distribution $\rho_0(\mathbf{x})$, target distribution $\rho_1(\mathbf{x})$ for MUOT testing.

Test	$\rho_0(\mathbf{x})$	$\rho_1(\mathbf{x})$
M1	$\rho_{MG}(\mathbf{x})$	$\hat{\rho}_G(\mathbf{x}, [0.5, 0.5, 0.5], 0.01 \cdot \mathbf{I})$
M2	$\hat{\rho}_G(\mathbf{x}, [0.5, 0.5, 0.5], 0.01 \cdot \mathbf{I})$	$\rho_{MG}(\mathbf{x})$

imbalance problem, in the process of mass merging (M1) and splitting (M2), the increase and decrease of mass is controlled by the source term ρg in the equation (6).

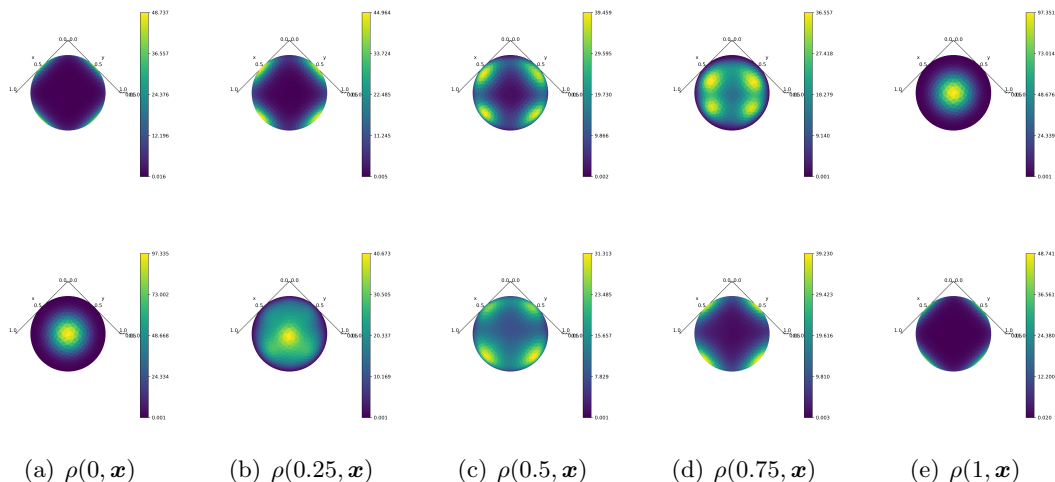


Figure 5.3.1: MUOT test on Sphere.

In addition, we give the values of the residuals of the equations for each loss function in all manifolds instances in Table 5.3.2. In our experiments, we set the stopping threshold, $\delta < 0.1$ or the number of iterations is less than 20000. In all cases, the residual reduce to a small level. However, for complicate surfaces, the residual may be relatively higher, especially for the residual of the continuous equation.

Table 5.3.2: Loss value for all Manifold examples.

Test	Manifold Examples			
	\mathcal{W}_M	\mathcal{L}_c	\mathcal{L}_{hj}	\mathcal{L}_{ic}
Sphere	1.40e1	9.93e-2	6.98e-2	3.87e-3
Ellipsoid	4.75e0	4.76e-1	9.35e-2	1.31e-3
Peanut	1.42e0	2.98e-1	8.64e-2	2.21e-2
Torus	8.82e0	1.21e-1	6.48e-2	1.06e-3
Opener	1.22e0	2.95e-1	8.62e-2	1.81e-3
M1	8.97e0	1.09e-1	8.21e-3	5.82e-4
M2	1.08e1	9.98e-2	7.70e-3	4.64e-4

5.4. Noisy Manifolds.

Now, we consider adding Gaussian noise to the point cloud to test the robustness of our algorithm. In this test, we use unit sphere and add Gaussian noise to points and associate normals respectively.

In this test, we use unit sphere and add noise to points and normals respectively. First, we add Gaussian noise to normals. The variance of noise is $\omega_n \sigma_n$ and σ_n is the variance of the normals. The perturbed normals are given in Figure 5.4.1. The associate results are shown in Figure 5.4.2.

When noise level is 1% and 5%, the transport phenomenon can still be captured. But when the noise is greater than 10%, our algorithm cannot continue to maintain this success.

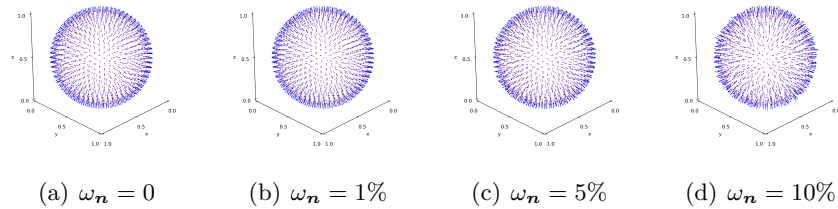


Figure 5.4.1: Normal vector with different level of noise.

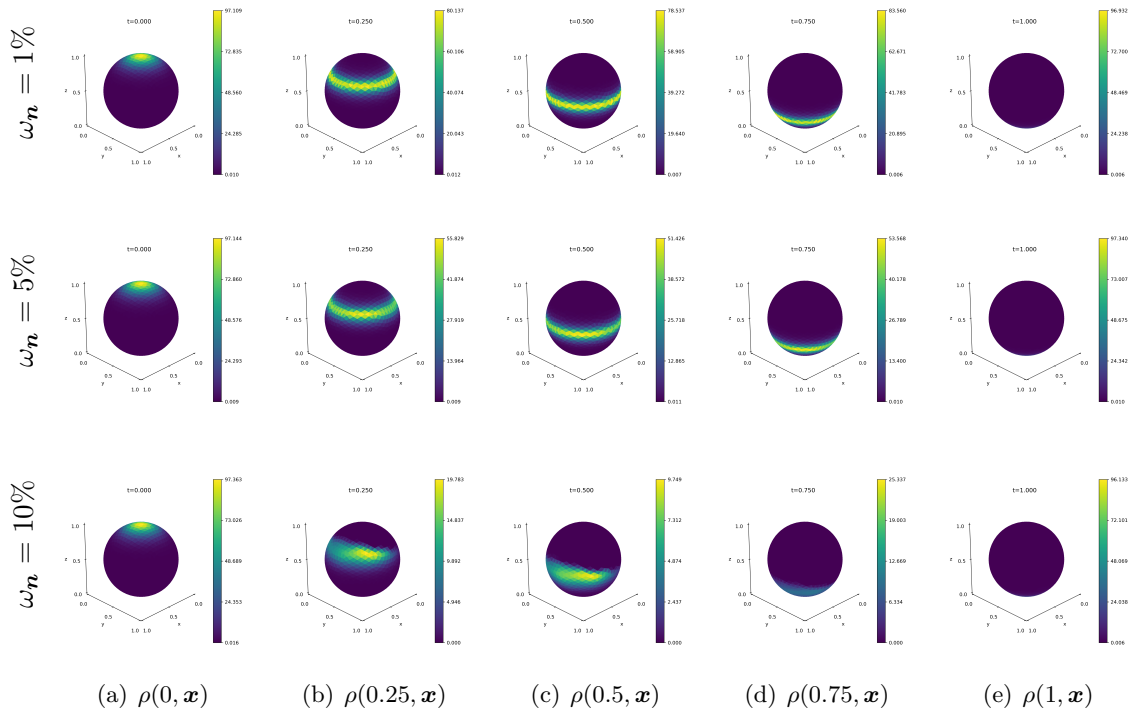


Figure 5.4.2: MOT test on sphere with different noise on normal vector.

The method is more sensitive to the perturbation on points. As shown in Figure 5.4.4, 5% noise is enough to make the method fail to give the true solution.

Finally, we add noise to both points and normal vectors, Figure 5.4.6. In this case, the performance is similar to points perturbed only case, only with 1% noise, the result is stable. Finally, we give the value of loss function in Table 5.4.1. With different noise level, 1%, 5%, 10%, the loss is comparable. But the results are completely change in high noise cases, due to the perturbation of points and normal vectors.

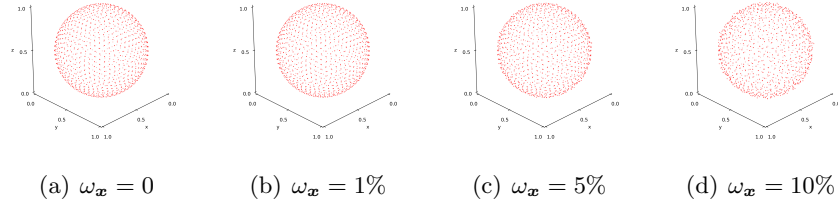


Figure 5.4.3: point cloud with different level of noise.

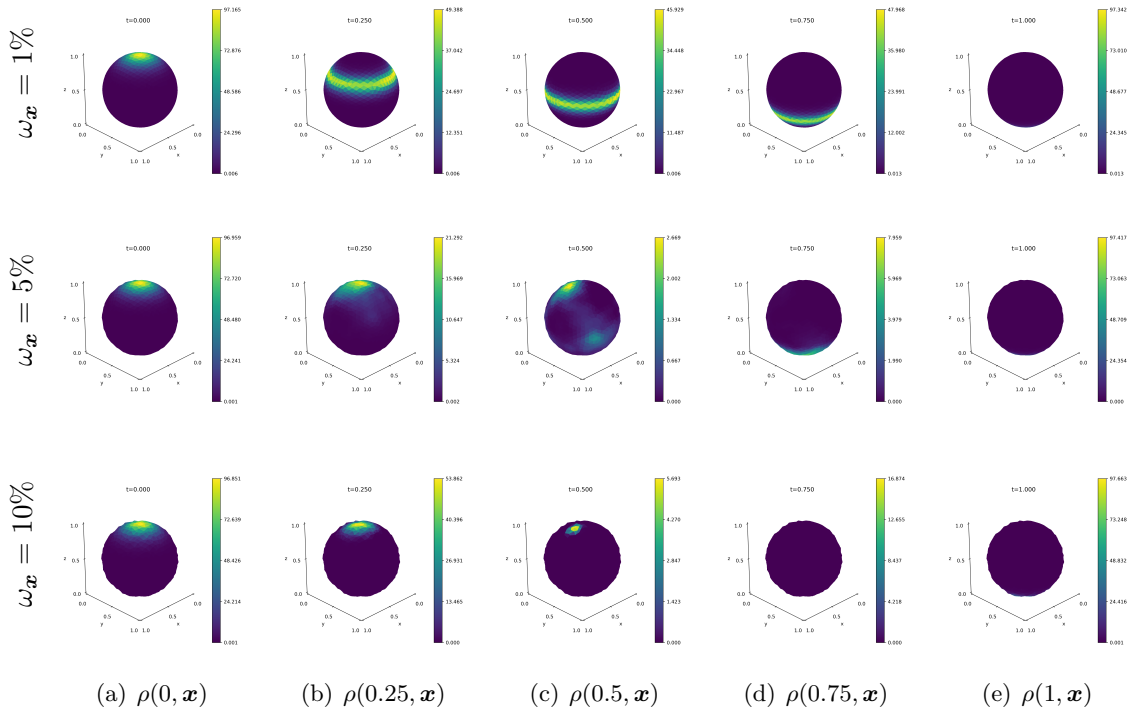


Figure 5.4.4: MOT test on sphere with different noise on point cloud.

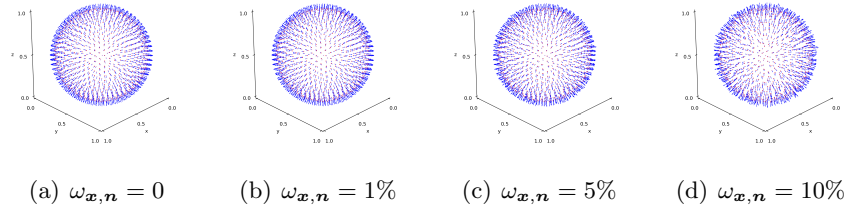


Figure 5.4.5: points and normal vector with different level of noise added to the sphere.

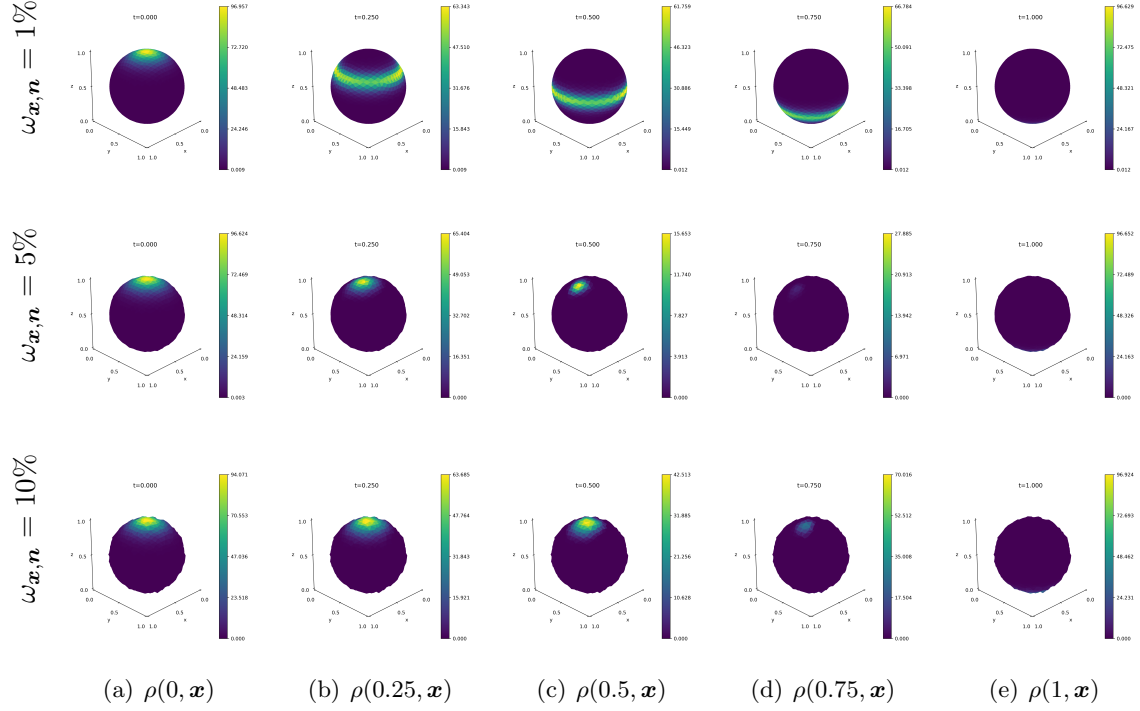


Figure 5.4.6: MOT test on sphere with different noise on both points and normal vectors.

Table 5.4.1: Loss value for different noise on sphere.

		1%	5%	10%
ω_n	\mathcal{W}_M	2.48e1	1.55e1	5.48e0
	\mathcal{L}_c	3.67e0	5.43e0	2.29e0
	\mathcal{L}_{hj}	7.29e-1	2.37e-1	7.49e-1
	\mathcal{L}_{ic}	4.81e-3	2.46e-3	1.67e-2
ω_x	\mathcal{W}_M	1.56e1	1.43e0	1.09e0
	\mathcal{L}_c	5.40e-1	9.87e-1	1.80e-1
	\mathcal{L}_{hj}	1.94e-1	8.82e-2	2.06e-2
	\mathcal{L}_{ic}	1.99e-2	2.05e-2	5.51e-3
$\omega_{x,n}$	\mathcal{W}_M	1.94e1	1.43e0	7.11e-1
	\mathcal{L}_c	4.30e0	1.05e0	2.10e0
	\mathcal{L}_{hj}	3.55e-1	1.69e-1	8.24e-2
	\mathcal{L}_{ic}	8.05e-2	2.95e-2	1.59e-2

5.5. Shape Transfer.

Finally, we apply our method on shape transfer problem. In shape transfer problem, the initial and terminal shape may have different mass, so unbalanced optimal transport provide a good model for this problem. We give three examples of shape transfer in Figure 5.5.1. All images are 28×28 in size. In our experiments, we choose the imbalance parameter $\eta = 2$, $\lambda_c = \lambda_{hj} = \lambda_{ic} = 1000$. And we use uniform point picking to sample 10 points at time t and 784 points on space (coordinate (x, y)).

For the first shape transfer example, the initial shape is a disc and we want to transfer it to a hexagram, as shown in the first row of Figure 5.5.1. In the second row, we show the result of transferring a triangle to a smiley face. The last example is the transfer between digit numbers which are extracted from MNIST dataset. In all tests, our method gives reasonable results to transfer shapes which demonstrate the effectiveness of the proposed method.

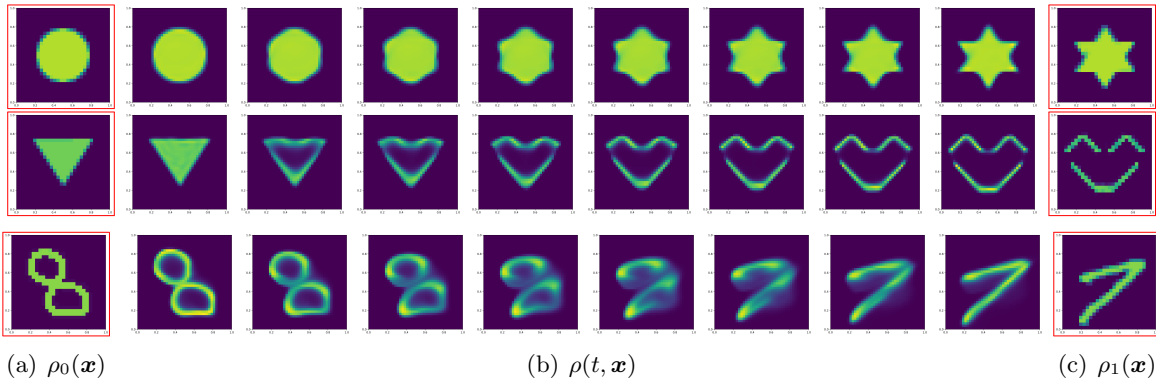


Figure 5.5.1: Shape transfer at different moments.

6. Conclusion

We propose a neural network-based method to solve UOT problem on point cloud. This method has good versatility and can save computational costs while avoiding mesh generation. Numerical experiments show that our method can effectively deal with MUOT problem. In current algorithm, the out normals of point cloud is also required. In the subsequent work, we will study the numerical method without explicitly given out normals.

Acknowledgments

This work is supported by National Natural Science Foundation of China (NSFC) No. 92370125 and No. 12301538.

References

- [1] Cédric Villani. *Topics in optimal transportation*, volume 58. American Mathematical Soc., 2021.

- [2] Thibault Séjourné, Gabriel Peyré, and François-Xavier Vialard. Unbalanced optimal transport, from theory to numerics. *Handbook of Numerical Analysis*, 24:407–471, 2023.
- [3] Nicolas Bonneel and Julie Digne. A survey of optimal transport for computer graphics and computer vision. In *Computer Graphics Forum*, volume 42, 2, pages 439–460. Wiley Online Library, 2023.
- [4] Jean Feydy, Benjamin Charlier, François-Xavier Vialard, and Gabriel Peyré. Optimal transport for diffeomorphic registration. In *Medical Image Computing and Computer Assisted Intervention- MICCAI 2017: 20th International Conference, Quebec City, QC, Canada, September 11-13, 2017, Proceedings, Part I 20*, pages 291–299. Springer, 2017.
- [5] Hongxing Qin, Yucheng Zhang, Zhentao Liu, and Baoquan Chen. Rigid registration of point clouds based on partial optimal transport. In *Computer Graphics Forum*, volume 41, 6, pages 365–378. Wiley Online Library, 2022.
- [6] Yimeng Chen, Yanyan Lan, Ruibin Xiong, Liang Pang, Zhiming Ma, and Xueqi Cheng. Evaluating natural language generation via unbalanced optimal transport. In *Proceedings of the Twenty-Ninth International Conference on International Joint Conferences on Artificial Intelligence*, pages 3730–3736, 2021.
- [7] Jie Li, Liwen Wu, Dan Xu, and Shaowen Yao. Arbitrary style transfer with attentional networks via unbalanced optimal transport. *IET Image Processing*, 16(7):1778–1792, 2022.
- [8] Frederike Lübeck, Charlotte Bunne, Gabriele Gut, Jacobo Sarabia del Castillo, Lucas Pelkmans, and David Alvarez-Melis. Neural unbalanced optimal transport via cycle-consistent semi-couplings. In *NeurIPS 2022 AI for Science: Progress and Promises*, 2022.
- [9] Gyri Reiersen, David Dao, Björn Lütjens, Konstantin Klemmer, Kenza Amara, Attila Steinegger, Ce Zhang, and Xiaoxiang Zhu. Reforestree: A dataset for estimating tropical forest carbon stock with deep learning and aerial imagery. In *Proceedings of the AAAI Conference on Artificial Intelligence*, volume 36, 11, pages 12119–12125, 2022.
- [10] Ting Sun, Bing Liu, Toshihiro Hasegawa, Zhiyi Liao, Liang Tang, Leilei Liu, Weixing Cao, and Yan Zhu. Sink-source unbalance leads to abnormal partitioning of biomass and nitrogen in rice under extreme heat stress: An experimental and modeling study. *European Journal of Agronomy*, 142:126678, 2023.
- [11] Gabriele Vissio, Valerio Lembo, Valerio Lucarini, and Michael Ghil. Evaluating the performance of climate models based on wasserstein distance. *Geophysical Research Letters*, 47(21):e2020GL089385, 2020.
- [12] Jie Li, Dan Xu, and Shaowen Yao. Sliced wasserstein distance for neural style transfer. *Computers & Graphics*, 102:89–98, 2022.
- [13] Hao Zhu, Chaoyou Fu, Qianyi Wu, Wayne Wu, Chen Qian, and Ran He. Aot: Appearance optimal transport based identity swapping for forgery detection. *Advances in Neural Information Processing Systems*, 33:21699–21712, 2020.

- [14] Jean Feydy, Pierre Roussillon, Alain Trouvé, and Pietro Gori. Fast and scalable optimal transport for brain tractograms. In *Medical Image Computing and Computer Assisted Intervention–MICCAI 2019: 22nd International Conference, Shenzhen, China, October 13–17, 2019, Proceedings, Part III 22*, pages 636–644. Springer, 2019.
- [15] Jean Feydy and Alain Trouvé. Global divergences between measures: from hausdorff distance to optimal transport. In *International Workshop on Shape in Medical Imaging*, pages 102–115. Springer, 2018.
- [16] Samuel Gerber, Marc Niethammer, Ebrahim Ebrahim, Joseph Piven, Stephen R Dager, Martin Styner, Stephen Aylward, and Andinet Enquobahrie. Optimal transport features for morphometric population analysis. *Medical Image Analysis*, 84:102696, 2023.
- [17] Gaspard Monge. Mémoire sur la théorie des déblais et des remblais. *Mem. Math. Phys. Acad. Royale Sci.*, pages 666–704, 1781.
- [18] Leonid V Kantorovich. On the translocation of masses. *Journal of mathematical sciences*, 133(4):1381–1382, 2006.
- [19] George B Dantzig. Application of the simplex method to a transportation problem. *Activity analysis and production and allocation*, 1951.
- [20] Jean-David Benamou and Yann Brenier. A computational fluid mechanics solution to the monge-kantorovich mass transfer problem. *Numerische Mathematik*, 84(3):375–393, 2000.
- [21] Wilfrid Gangbo, Wuchen Li, Stanley Osher, and Michael Puthawala. Unnormalized optimal transport. *Journal of Computational Physics*, 399:108940, 2019.
- [22] Wonjun Lee, Rongjie Lai, Wuchen Li, and Stanley Osher. Fast algorithms for generalized unnormalized optimal transport, 2019.
- [23] Wonjun Lee, Rongjie Lai, Wuchen Li, and Stanley Osher. Generalized unnormalized optimal transport and its fast algorithms. *Journal of Computational Physics*, 436:110041, 2021.
- [24] Alain Bensoussan, Jens Frehse, Phillip Yam, et al. *Mean field games and mean field type control theory*, volume 101. Springer, 2013.
- [25] René Carmona, François Delarue, et al. *Probabilistic theory of mean field games with applications I-II*. Springer, 2018.
- [26] Jean-Michel Lasry and Pierre-Louis Lions. Mean field games. *Japanese journal of mathematics*, 2(1):229–260, 2007.
- [27] Samuel Gerber, Marc Niethammer, Martin Styner, and Stephen Aylward. Exploratory population analysis with unbalanced optimal transport. In *Medical Image Computing and Computer Assisted Intervention–MICCAI 2018: 21st International Conference, Granada, Spain, September 16-20, 2018, Proceedings, Part III 11*, pages 464–472. Springer, 2018.
- [28] Thomas Gallouët, Maxime Laborde, and Leonard Monsaingeon. An unbalanced optimal transport splitting scheme for general advection-reaction-diffusion problems. *ESAIM: Control, Optimisation and Calculus of Variations*, 25:8, 2019.

- [29] Stanislav Kondratyev and Dmitry Vorotnikov. Convex sobolev inequalities related to unbalanced optimal transport. *Journal of Differential Equations*, 268(7):3705–3724, 2020.
- [30] Ryoma Sato, Makoto Yamada, and Hisashi Kashima. Fast unbalanced optimal transport on a tree. *Advances in neural information processing systems*, 33:19039–19051, 2020.
- [31] Khiem Pham, Khang Le, Nhat Ho, Tung Pham, and Hung Bui. On unbalanced optimal transport: An analysis of sinkhorn algorithm. In *International Conference on Machine Learning*, pages 7673–7682. PMLR, 2020.
- [32] Laetitia Chapel, Rémi Flamary, Haoran Wu, Cédric Févotte, and Gilles Gasso. Unbalanced optimal transport through non-negative penalized linear regression. *Advances in Neural Information Processing Systems*, 34:23270–23282, 2021.
- [33] Da Li, Michael P Lamoureux, and Wenyuan Liao. Application of an unbalanced optimal transport distance and a mixed l1/wasserstein distance to full waveform inversion. *Geophysical Journal International*, 230(2):1338–1357, 2022.
- [34] Martin Bauer, Emmanuel Hartman, and Eric Klassen. The square root normal field distance and unbalanced optimal transport. *Applied Mathematics & Optimization*, 85(3):35, 2022.
- [35] Thibault Séjourné, François-Xavier Vialard, and Gabriel Peyré. Faster unbalanced optimal transport: Translation invariant sinkhorn and 1-d frank-wolfe. In *International Conference on Artificial Intelligence and Statistics*, pages 4995–5021. PMLR, 2022.
- [36] Florian Beier, Johannes von Lindheim, Sebastian Neumayer, and Gabriele Steidl. Unbalanced multi-marginal optimal transport. *Journal of Mathematical Imaging and Vision*, 65(3):394–413, 2023.
- [37] Fei Wang, Mengqing Jiang, Chen Qian, Shuo Yang, Cheng Li, Honggang Zhang, Xiaogang Wang, and Xiaoou Tang. Residual attention network for image classification. In *Proceedings of the IEEE conference on computer vision and pattern recognition*, pages 3156–3164, 2017.
- [38] Waseem Rawat and Zenghui Wang. Deep convolutional neural networks for image classification: A comprehensive review. *Neural computation*, 29(9):2352–2449, 2017.
- [39] Dengsheng Lu and Qihao Weng. A survey of image classification methods and techniques for improving classification performance. *International journal of Remote sensing*, 28(5):823–870, 2007.
- [40] William Chan, Navdeep Jaitly, Quoc Le, and Oriol Vinyals. Listen, attend and spell: A neural network for large vocabulary conversational speech recognition. In *2016 IEEE international conference on acoustics, speech and signal processing (ICASSP)*, pages 4960–4964. IEEE, 2016.
- [41] Li Deng, Geoffrey Hinton, and Brian Kingsbury. New types of deep neural network learning for speech recognition and related applications: An overview. In *2013 IEEE international conference on acoustics, speech and signal processing*, pages 8599–8603. IEEE, 2013.
- [42] Ossama Abdel-Hamid, Abdel-rahman Mohamed, Hui Jiang, Li Deng, Gerald Penn, and Dong Yu. Convolutional neural networks for speech recognition. *IEEE/ACM Transactions on audio, speech, and language processing*, 22(10):1533–1545, 2014.

- [43] Yoav Goldberg. A primer on neural network models for natural language processing. *Journal of Artificial Intelligence Research*, 57:345–420, 2016.
- [44] Yoav Goldberg. *Neural network methods for natural language processing*. Springer Nature, 2022.
- [45] Ronan Collobert and Jason Weston. A unified architecture for natural language processing: Deep neural networks with multitask learning. In *Proceedings of the 25th international conference on Machine learning*, pages 160–167, 2008.
- [46] Yaohua Zang, Gang Bao, Xiaojing Ye, and Haomin Zhou. Weak adversarial networks for high-dimensional partial differential equations. *Journal of Computational Physics*, 411:109409, 2020.
- [47] Bing Yu et al. The deep ritz method: a deep learning-based numerical algorithm for solving variational problems. *Communications in Mathematics and Statistics*, 6(1):1–12, 2018.
- [48] Maziar Raissi, Paris Perdikaris, and George E Karniadakis. Physics-informed neural networks: A deep learning framework for solving forward and inverse problems involving nonlinear partial differential equations. *Journal of Computational physics*, 378:686–707, 2019.
- [49] Haoqiang Fan, Hao Su, and Leonidas J Guibas. A point set generation network for 3d object reconstruction from a single image. In *Proceedings of the IEEE conference on computer vision and pattern recognition*, pages 605–613, 2017.
- [50] Karol Gregor, Ivo Danihelka, Alex Graves, Danilo Rezende, and Daan Wierstra. Draw: A recurrent neural network for image generation. In *International conference on machine learning*, pages 1462–1471. PMLR, 2015.
- [51] Yaniv Taigman, Adam Polyak, and Lior Wolf. Unsupervised cross-domain image generation. *arXiv preprint arXiv:1611.02200*, 2016.
- [52] Karren D Yang and Caroline Uhler. Scalable unbalanced optimal transport using generative adversarial networks. In *International Conference on Learning Representations*, 2018.
- [53] John Lee, Nicholas P Bertrand, and Christopher J Rozell. Unbalanced optimal transport regularization for imaging problems. *IEEE Transactions on Computational Imaging*, 6:1219–1232, 2020.
- [54] Zhiheng Ma, Xing Wei, Xiaopeng Hong, Hui Lin, Yunfeng Qiu, and Yihong Gong. Learning to count via unbalanced optimal transport. In *Proceedings of the AAAI Conference on Artificial Intelligence*, volume 35, 3, pages 2319–2327, 2021.
- [55] Quoc Cuong Le, Donatello Conte, and Moncef Hidane. Unbalanced optimal transport in multi-camera tracking applications. In *Pattern Recognition. ICPR International Workshops and Challenges: Virtual Event, January 10–15, 2021, Proceedings, Part V*, pages 327–343. Springer, 2021.
- [56] Kilian Fatras, Thibault Sejourne, Remi Flamary, and Nicolas Courty. Unbalanced minibatch optimal transport; applications to domain adaptation. In *International Conference on Machine Learning*, pages 3186–3197. PMLR, 2021.

- [57] Kai Cao, Qiyu Gong, Yiguang Hong, and Lin Wan. A unified computational framework for single-cell data integration with optimal transport. *Nature Communications*, 13(1):7419, 2022.
- [58] Xin Shen, Wai Lam, Shumin Ma, and Huadong Wang. Joint learning of text alignment and abstractive summarization for long documents via unbalanced optimal transport. *Natural Language Engineering*, pages 1–29, 2023.
- [59] Henri De Plaen, P De Plaen, J Suykens, M Proesmans, T Tuytelaars, and L Van Gool. Unbalanced optimal transport: A unified framework for object detection. In *Proceedings/CVPR, IEEE Computer Society Conference on Computer Vision and Pattern Recognition. IEEE Computer Society Conference on Computer Vision and Pattern Recognition*. IEEE, 2023.
- [60] Jun Dan, Tao Jin, Hao Chi, Shunjie Dong, and Yixuan Shen. Uncertainty-guided joint unbalanced optimal transport for unsupervised domain adaptation. *Neural Computing and Applications*, 35(7):5351–5367, 2023.
- [61] Hugo Lavenant, Sebastian Claici, Edward Chien, and Justin Solomon. Dynamical optimal transport on discrete surfaces. *ACM Transactions on Graphics (TOG)*, 37(6):1–16, 2018.
- [62] Jiajia Yu, Rongjie Lai, Wuchen Li, and Stanley Osher. Computational mean-field games on manifolds. *Journal of Computational Physics*, 484:112070, 2023.
- [63] Richard D Neidinger. Introduction to automatic differentiation and matlab object-oriented programming. *SIAM review*, 52-3:545–563, 2010.
- [64] Diederik P Kingma and Jimmy Ba. Adam: A method for stochastic optimization. *arXiv preprint arXiv:1412.6980*, 2014.
- [65] Kun Xu, Wei-Lun Sun, Zhao Dong, Dan-Yong Zhao, Run-Dong Wu, and Shi-Min Hu. Anisotropic spherical gaussians. *ACM Transactions on Graphics (TOG)*, 32(6):1–11, 2013.